

---

# BRULÉ: Barycenter-Regularized Unsupervised Landmark Extraction

---

Iaroslav Bespalov, Nazar Buzun, Dmitry V. Dylov

Skolkovo Institute of Science and Technology, Bolshoy blvd., 30/1, Moscow 121205, Russia  
{iaroslav.bespalov, n.buzun, d.dylov}@skoltech.ru

## Abstract

Unsupervised retrieval of image features is vital for many computer vision tasks where the annotation is missing or scarce. In this work, we propose a new unsupervised approach to detect the landmarks in images, and we validate it on the popular task of human face key-points extraction. The method is based on the idea of auto-encoding the wanted landmarks in the latent space while discarding the non-essential information in the image and effectively preserving the interpretability. The interpretable latent space representation is achieved with the aid of a novel two-step regularization paradigm. The first regularization step evaluates transport distance from a given set of landmarks to the average value (the barycenter by Wasserstein distance). The second regularization step controls deviations from the barycenter by applying random geometric deformations synchronously to the initial image and to the encoded landmarks. During decoding, we add style features generated from the noise and reconstruct the initial image by the generative adversarial network (GAN) with transposed convolutions modulated by this style. We demonstrate the effectiveness of the approach both in unsupervised and in semi-supervised training scenarios using the 300-W and the CelebA datasets. The proposed regularization paradigm is shown to prevent overfitting, and the detection quality is shown to improve beyond the supervised outcome.

## 1 Introduction

Our study of the unsupervised landmark detection began with the question of whether it is possible to store the image landmarks within the bottleneck of an auto-encoder. How can we influence the auto-encoder to contain *only* the information about the image landmarks in its bottleneck and what kind of regularization would be required for that? These questions, along with the fact that the landmarks of the same class typically look similar (e.g., key-points extracted from different faces resemble each other), have led us to the idea of comparing the post-encoder features with some 'average' landmarks.

Using auto-encoders to extract landmarks is similar to the principle of unsupervised segmentation, because it is in the bottleneck where the features of the segmentation contours could be distilled. Image segmentation has been a desirable task in the field of deep learning over the last five years [4, 9, 33, 5]. Today, the state-of-the-art algorithms show impressive results but, oftentimes, require massive amounts of annotated data, which is not always available [9, 33, 5]. Reducing the required amount of labelled data for the segmentation algorithms is a task of pressing demand, which has been the other motivation for our study. Instead of complex segmentation patterns, we begin with the unsupervised detection of key-points in the human faces, which will be the main focus of this paper.

If the 'average' landmarks pattern needs to be computed, it makes sense to calculate it via the optimal transport distance [1], also known as the *barycenter*. Wasserstein barycenters rose in popularity in

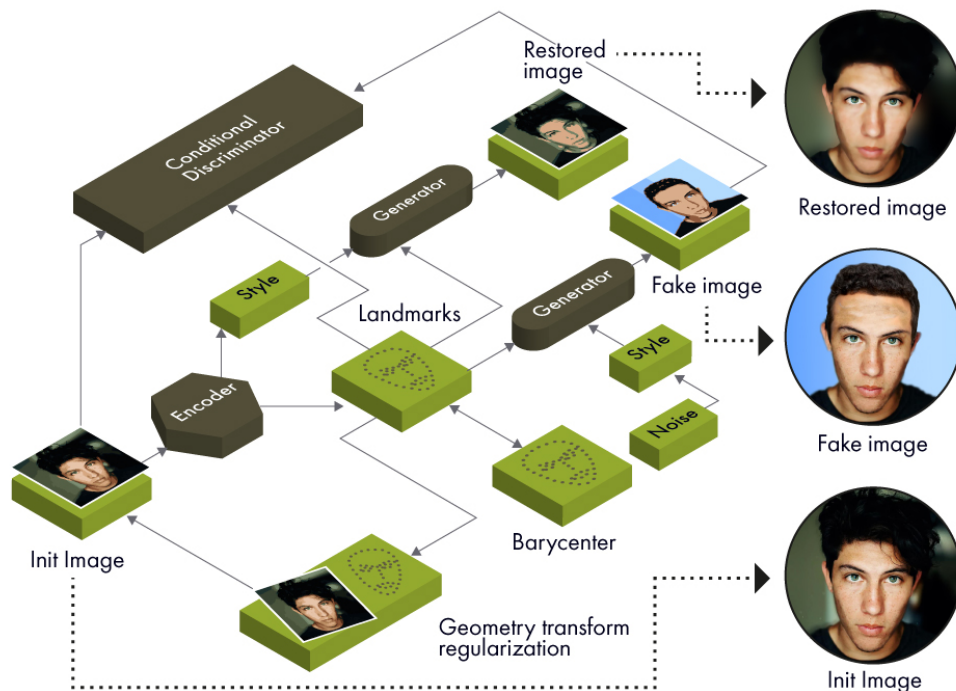


Figure 1: BRULÉ: Barycenter-Regularized Unsupervised Landmark Extraction. Principal diagram. The first restoration generates style data from random noise and subsequently forwards it to GAN. The second restoration predicts the style and landmarks from the initial image and applies the same adversarial generator. The initial and the restored images are compared by conditional discriminator and the  $L_1$  norm. Wasserstein-2 distance keeps the encoded landmarks close to the barycenter. The image and its predicted landmarks are synchronously deformed via affine and elastic geometric transforms. Finally, one predicts the landmarks of the transformed image and compares them to the transformed landmarks.

recent years as they preserve common topological properties of geometrical figures set in the wide range of tasks [1, 2, 24].

In this work, we extend their use for the regularization in the landmark detection problem. Once computed, the barycenter of landmarks could be used for calculating distances to the rest of the predicted (encoded) landmarks.

The principal architecture is illustrated in Figure 1. Besides barycenter regularization we involve regularization by geometric transforms [26], that allows to control deviations from the barycenter and synchronize coordinates of image and landmarks. For decoding we use generative neural network. More details of the method are described in Section 2 below. Overall, the contribution of this paper is in the following:

- The first method that predicts comprehensible landmarks in unsupervised way with interpretability. Works in semi-supervised scenario too, *outperforming state-of-the-art methods*;
- Regularization by the Wasserstein distance to the barycenter, factorized by three types of transformations;
- New type of cyclic GAN architecture [34] that performs training with only one domain data and decomposes images into landmarks and style;
- Extended architecture of stylegan2 [15] to conditional image generation.

**Related work.** Traditionally, the algorithms of the unsupervised segmentation extract latent representations via deep autoencoders [30, 13, 14]. These methods attempt to form clusters of the latent pixels which correspond to correlated parts of the initial image. To guarantee direct correspondence between image and segmentation coordinates, the authors in [13] suggested the idea of regularization using geometry transformations, expressed as a condition  $L(gI) = gL(I)$ , where  $I$  is the image,  $g$  is some deformation, and  $L$  is a segmentation mapping. *Generative adversarial networks*, such as SEIGAN [19], were also proposed for unsupervised segmentation, relying on the latent space representation, segment painting, and object embedding into another background (with the constraint that the image must remain realistic).

There are many landmark detection approaches, especially for faces. Initially, they were based on various statistical approaches, preprocessing, and enhancements [6, 16, 7]. Rapid progress of deep learning then instigated a series of supervised methods: cascade of CNNs [25], multi-task learning (pose, smile, the presence of glasses, sex of person) [32], and recurrent attentive-refinements via Long Short-Term Memory networks (LSTMs) [31]. Special loss functions (e.g., wing loss [8]) were shown to further improve the accuracy of CNN-based facial landmark localisation.

*Unsupervised pre-training* has seen major interest in the community with the advent of data-hungry deep networks. A classic approach for such a task is the use of autoencoders, comprising different variations of embeddings [11, 27, 26]. Papers [11] and [29] use the condition  $I_2 = G(I_1, L(I_2))$  and the additional condition of sparsity on the heatmap corresponding to  $L(I_2)$ . If images  $I_1$  and  $I_2$  have different landmarks but have the same style (e.g., sequential frames from the video), the network  $G$  can generate  $I_2$  from  $I_1$  and the landmarks  $L(I_2)$ . Method [12] is similar, but it has an additional discriminator network to compare predicted landmarks to the landmarks from the dataset by distribution. Big drawback of these methods is the necessity to have paired images or video datasets. Another class of methods, such as [27], [28], and [26], does employ the geometric transformations for regularization. However, these works lose the landmarks interpretability in the process. Besides, their unsupervised nature was only implemented as a pertaining step for landmark detection.

In our work, we have chosen Wasserstein distance because it can establish pairwise correspondence between predicted landmarks and the key-points of the barycenter. It makes the regularizer more flexible, enabling the capability of comparing the landmark sets of different size and order. We refer to work [1] that describes projection of 3D figures into the barycenter coordinates, and the theoretical study of the barycenters in [2, 24].

## 2 Method

The training process of the unsupervised landmark detector, illustrated in Figure 1, consists of two main steps: conditional GAN training [34, 21] and the actual landmark detection optimisation. These two steps are repeated every training iteration. When the encoder network predicts the heatmap of landmarks  $L$  of the batch of images  $I$ , one applies the optimisation routine to the generator ( $G$ ) and discriminator ( $D$ ) networks. Let  $S_o$  denote the network that maps the Gaussian noise vector  $z$  to a random style, and  $S$  – the network that maps images (either fake or real) to their style.

---

### Algorithm 1: Single iteration of conditional GAN optimisation

---

```

sample noise:  $\forall k : z_k \sim \mathcal{N}(0, 1)$ ;
initialize  $g$ : random geometric transformation (affine or warp);
generate fake image:  $I_F = G(gL, S_o(z))$ ;
max discriminator loss:  $-\mathbb{E} \log(1 + e^{-D(gI, gL)}) - \mathbb{E} \log(1 + e^{D(I_F, gL)})$ ;
if iteration mod 4 = 0 then
    | min discriminator penalty :  $\lambda \mathbb{E} \|\nabla D(gI, gL)\|^2$ ;
end
min generator loss:  $\mathbb{E} \log(1 + e^{-D(I_F, gL)})$ ;
if iteration mod 5 = 0 then
    | restore image:  $I_R = G(gL, S(I))$ ;
    | landmarks of fake:  $L_F = L(I_F)$ ;
    | style of fake:  $S_F = S(I_F)$ ;
    |  $\min_{G, S} \{c_1 \|I_R - gI\|_1 + c_2 H(L_F \|gL) + c_3 \mathcal{L}_{\text{style}}(S_F)\}$ ;
end

```

---

The training paradigm of Algorithm 1 starts similarly to MUNIT [10], where one encodes the style and the landmarks from an input image. Then, we separately restore the image and generate the fake. It makes GAN training more stable and allows to decompose the image into content and style, with the role of content being played by the landmarks. The loss function for discriminator and generator enhances that from `stylegan2` [15], where the penalty of discriminator enforces smoother separation of classes (fake and real images). In generator optimization we combine the original generator loss with the  $\mathcal{L}_1$  loss between restored and initial images. We also add a term that computes cross-entropy  $H(L_F \| gL)$  between the landmarks from the fake and from the initial image, which introduces important constraint for conditional generation only (in addition to the conditional discriminator). Random geometric transforms ( $g$ ) improves coordinates synchronisation of  $L$ ,  $I_R$  and  $I_F$ . We train the GAN together with the style encoder. The last loss element  $\mathcal{L}_{\text{style}}$  is necessary for the style adjustments, assuring that the style of the fake looks similar to both the generated style  $S_o(z)$  and to that of the transformed fake  $S(gI_F)$ .

---

**Algorithm 2:** Single iteration of landmarks encoder optimization

---

initial image as input:  $I$ ;  
heatmap of landmarks:  $L = L(I)$ ;  
coordinates of landmarks:  $X_L$ ;  
sparse heatmap of landmarks:  $L_{\text{sp}} \sim \exp\{-\|\text{mesh} - X_L\|^2/2\}$ ;  
initialize  $g$ : random geometric transformation;  
generate fake:  $I_F = G(L, S_o(z))$ ;  
restore image:  $I_R = G(L_{\text{sp}}, S(I))$ ;  
update parameters of landmarks encoder by the following loss:  
 $\min_L \{c_5 \mathcal{R}_b(X_L) + c_6 \mathcal{R}_g(L) + c_7 H(L \| L_{\text{sp}}) + c_8 \mathcal{L}_D(L) + c_9 \|I_R - I\|_1 + c_{10} H(L(I_F) \| L)\}$ ;

---

Such encoder training is enabled every third iteration. The resulting landmarks, produced by the encoder, are a heatmap, the entropy of which  $H(L \| L_{\text{sp}})$  we want to reduce to concentrate around their mean values (minimization of cross-entropy yields a mixture of Gaussian measures  $L_{\text{sp}}$ , with their centers being located in the coordinates of the landmarks  $X_L$ ). Also, the encoder is optimised by the landmark’s participation in the generation of the fake and the restored images. Regularizers  $\mathcal{R}_b$  (distance to the barycenter),  $\mathcal{R}_g$  ( $g$ -transform synchronisation), and  $\mathcal{L}_D$  (influence of the GAN) are described in Section 4.

**Hyperparameters tuning.** The coefficients (hyperparameters) of the loss of the landmarks encoder are tuned on a validation dataset. The tuning procedure uses the gradient-free optimization. We choose a random uniform direction in the hyperparameter space and minimize the validation score (defined in Section 5) along this direction using the golden-section search [20], repeating it multiple times. If a given direction does not improve the score in the initial two points of the golden-section search, a new one is sampled several times, with the best one being selected. The gradient-free optimization was chosen thanks to its relatively low computational cost in this problem, and thanks to its ability to aggregate updates of network weights during more than one iterations.

### 3 Architecture description

To build the conditional GAN for our purpose, we enhance the `stylegan2` architecture [15] by introducing the following modifications to the original generator and discriminator (see Fig. 2).

**Generator.** We consecutively upsample and downsample the heatmap of the landmarks from the size  $64 \times 64$  to the sizes  $[4 \times 4, 8 \times 8, \dots, 256 \times 256]$ , and then, we concatenate them with the outputs from the progression of the modulated convolution blocks. At the same time, the noise passes through a series of linear layers to place the style on the manifold, which helps them to acquire the same topological properties as the images in the dataset. These styles are further used in `ModulatedConvBlock` to obtain the corresponding weights.

**Discriminator.** In the discriminator, we connect by channels the landmarks with the intermediate layer, obtained from the input images.

**Landmark Encoder.** Our Landmarks encoder consists of two principal parts. Due to recent success of the stacked hourglass model [18], we have integrated it in our landmarks encoder, which produces

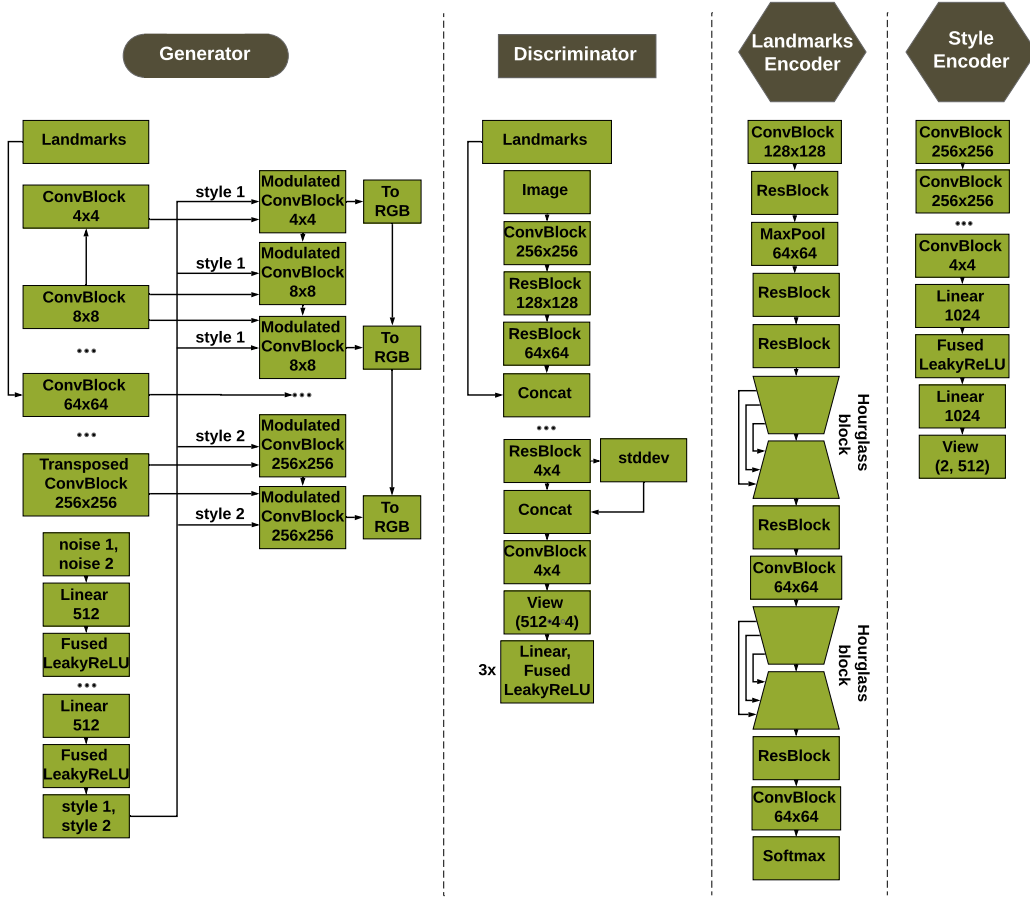


Figure 2: Complete architecture. ConvBlock is a combination of convolution layer and LeakyReLU. Blocks FusedLeakyReLU, ModulatedConvBlock, ToRGB are borrowed from stylegan2 [15]. Dimensions below the block names correspond to the size of output tensors.

a heatmap with separate channels corresponding to key-point probabilities. Applying softmax to each channel, makes the total probability of each point equal to one.

**Style Encoder.** Style encoder is just a regular CNN.

#### 4 Loss function

The loss function for our architecture contains 6 components, with each component having its own *physical* meaning. We will now discuss each of them in detail.

**Barycenter regularizer.** If the landmark encoder predicts the landmarks  $L$  at coordinates  $X_L$ , the transport path from  $X_L$  to the barycenter  $X_b$  entails two principal transformations: the linear (affine) and the nonlinear (warping). Hence, the transport mapping is expressed as sequential translation, two other affine transformations (rotation and scaling), and the nonlinear elastic deformation<sup>1</sup>:

$$\mathcal{R}_b(X_L) = c_{11}W_2^2(X_L, T[X_L]) + c_{12}W_2^2(T[X_L], AT[X_L]) + c_{13}W_2^2(AT[X_L], X_b),$$

where  $W_2^2$  is the Wasserstein-2 distance [1],  $T$  is the translation operator,  $A$  is the affine operator (rotation and scaling). Each of these three terms is included with its own coefficient to vary the

<sup>1</sup>We find expressing the translation term separately from the other affine transformations to be useful due to its bigger impact on the regularization.

strength of the regularization accordingly. Naturally, simpler deformations are preferred, yielding lower coefficients by the corresponding terms.

The translation  $T[X_L]$  is determined by the center of mass difference between  $X_L$  and  $X_b$ . Conventionally, it is tempting to express the affine matrix  $A$  via the covariance matrix  $\Sigma$ ; however, it would give a solution with an accuracy up to any orthogonal matrix, because  $\Sigma = A A^T$  and one might inject the orthogonal transformation between  $A$  and  $A^T$ . It is possible to resolve this irregularity by establishing a pairwise correspondence between the source and the destination of the linear transport mapping. Namely, if  $P$  is a probability matrix of the complete transport plan, such that  $P_{ij}$  is the probability that  $i$ -th point from  $X_L$  moves to  $j$ -th point of  $X_b$ , one can find the matrix of affine operator  $A$  by solving the following optimization problem:

$$\min_A \left\{ \sum_{ij} P_{ij} \|AX_L[i] - X_b[j]\|^2 \right\}, \text{ yielding the solution: } A = \left( X_L^T \text{diag}(P\mathbf{1}) X_L \right)^{-1} X_L^T P X_b.$$

**Geometric regularizer.** To guarantee correspondence of coordinates of the landmarks to those in the image, we add a proper geometric regularization. The geometric regularization assures that the same affine and elastic transformations are applied both to the original image  $I$  and to the predicted landmarks  $L$ . After applying the deformations  $g$ , we use the encoder to predict a new set of landmarks  $L(gI)$  in the transformed image  $gI$ . This loss component minimizes cross-entropy between  $L(gI)$  and  $gL$ , along with the  $L_1$  distance between their coordinates:

$$\mathcal{R}_g(L(gI)) = H(L(gI) \| gL) + \|X_L(gI) - X_{gL}\|_1.$$

**Landmarks and style decorrelation.** Obviously, the generator  $G$ , fed with the sets of absolutely the same landmarks but with different styles, should create semantically similar images. Hence, we generate two fakes for the same set of landmarks with two different styles  $S_1$  and  $S_2$ , and then, minimize  $L_1$  norm between the landmarks of the produced fakes:

$$\mathcal{L}_{decor}(L, S_1, S_2) = \|L(G[L, S_1]) - L(G[L, S_2])\|_1.$$

**Reconstruction.** This term compares the original image to the reconstructed one, for a given set of landmarks and the encoded style produced by the generator:

$$\mathcal{L}_{rec}(L) = \|G[L, S(I)] - I\|_1.$$

**Discriminator loss.** We further increase correlation between the image and the landmarks by chaining with the GAN generator losses:

$$\mathcal{L}_D(L) = \mathbb{E} \log \left( 1 + e^{-D(I, L)} \right) + \mathbb{E} \log \left( 1 + e^{-D(I_F, L)} \right).$$

**Style consistency.** We make style consistent with the style generated from noise and make it invariant to the geometric transformations:

$$\mathcal{L}_{style}(S) = \|S - S_o(z)\|_1 + \|S - S(gI)\|_1.$$

## 5 Experiments

We consider two popular face datasets: CelebA [17] and 300-W [22]. The former lacks ground-truth landmarks and the latter contains 68 annotated key-points per face, with 3k training pairs in total. These datasets are quite similar, but the scale of images is somewhat different, providing a good setting for testing the robustness and universality of our method. As described above, we aspire to accomplish a completely *unsupervised* extraction of landmarks using the BRULÉ framework; but we also demonstrate efficacy in the *semi-supervised* training scenario so that we can compare to the state-of-the-art methods.

**Unsupervised experiments.** In the unsupervised scenario, we first compute the barycenter using the given landmarks from the 300-W dataset. We stress that this initiation does not contradict the criteria for being unsupervised, because by doing so we essentially only 'show' the object of interest to the

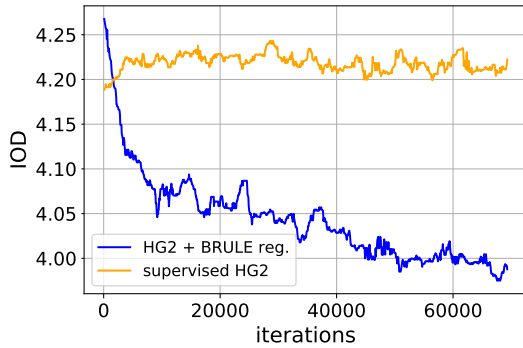


Figure 3: Supervised training on 300-W dataset. Orange line shows inter ocular distance (IOD) for HG2 [18] model during training process from a pretrained state. Blue line corresponds to training the same model, but with our regularization ( $\mathcal{L}_D$ , and  $H(L(I_F)\|L)$ ).

Method	Training	IOD, %
TCDCN [32]	sup.	5.54
RAR [31]	sup.	4.94
WingLoss [8]	sup.	4.04
<b>BRULÉ</b>	<b>semi-sup.</b>	<b>3.90 ± 0.07</b>
Sparse [27]	un. pretr.	7.97
Fab-Net [29]	un. pretr.	5.71
UDIT [12]	un. pretr.	5.37
Dense 3D [28]	un. pretr.	8.23
<b>DVE HG [26]</b>	<b>un. pretr.</b>	<b>4.65</b>
<b>BRULÉ</b>	<b>unsup.</b>	<b>6.64 ± 0.32</b>

Table 1: Quantitative comparison on the 300-W dataset using the inter ocular distance (IOD) as the metric. Training: ‘sup.’ = fully supervised; ‘semi-sup.’ = CelebA used to train GAN; ‘un. pretr.’ = CelebA pretrains encoder only (“semi-supervised”); ‘unsup.’ = unsupervised.

model. Once computed, the barycenter is kept fixed for all experiments. The training follows the recipe from Section 2, with the Algorithm 1 hyperparameters being set to  $c_1 = 30$ ,  $c_2 = 10^4$ ,  $c_3 = 30$ , and  $\lambda = 80$ . The automatically tuned hyperparameters in Algorithm 2 are initiated as:  $c_5 = 20$ ,  $c_6 = 20$ ,  $c_7 = 10^5$ ,  $c_8 = 5$ ,  $c_9 = 10$  and  $c_{10} = 1$ . Parameters in  $R_b$  are:  $c_{11} = 1$ ,  $c_{12} = 1$ , and  $c_{13} = 1$ . The error values of the landmark prediction were evaluated on the standard test set of 300-W, using a conventional metric – the inter ocular distance (IOD) [3]. However, during the training, instead of the Euclidean norm like in the other works, we used the Wasserstein  $W_1$  distance [1] between the predicted and the ground truth landmarks (divided by the distance between the key-points corresponding to the outer eye corners), because the key-points lack the pairwise correspondence. The chosen metric for the test set (IOD) was identical for all methods in our comparison.

Performance of our method is demonstrated in Figure 4 and the comparison against the state-of-the-art methods is summarized in Table 1. Training of the model takes three days on three V100 Tesla GPUs, which is of the same order of magnitude as the other models in Table 1, as well as the rest of



Figure 4: Unsupervised BRULÉ. *Top two rows*: real images with predicted landmarks. *Bottom row*: conditionally generated GAN images from the same landmarks as the ones directly above. Examples include both successful cases and the especially difficult ones (e.g., the person looking sideways).



Figure 5: Semi-supervised BRULÉ. *Top row*: real images with predicted landmarks. Our regularization improves the detection both quantitatively (see Table 1) and perceptually. *Bottom row*: fake images generated by conditional GAN with the same landmarks as in images above and a given style.

architectures that utilize `stylegan`-like frameworks. Additional details about training and evaluation are given in the Supplementary materials.

**Semi-supervised experiments.** In the ‘semi-supervised’ case, we have trained the GAN part (i.e., Algorithm 1) on CelebA and the landmarks encoder on 300-W. The barycenter regularisation has been excluded from the loss function because it is meaningless to complement the true known landmarks with the ‘average’ ones that come from the barycenter<sup>2</sup>. Intuitively, the barycenter regularizer is efficient only on limited training sets with missing annotations. If the true labels are available, it has a limited effect, and the BRULÉ pipeline acts as generic regularizer, which increases training stability and reduces overfitting, as shown in Figures 3 and 5.

**Discussion.** Face landmarks predicted by our unsupervised method, as illustrated in Figure 4, are very good outcomes, especially in the examples with the faces photographed from the front. Because this is the predominant orientation of the face in both datasets, the barycenter really ‘looks’ like the frontal photograph. Some problems emerge when the testing images are acquired from the side-view, probably requiring larger warp deformations or more complex affine transformations to compensate for the ‘ruined’ orientation. In the first version of BRULÉ, precise detection of the landmarks seems to be possible in the local vicinity of the barycenter because of the weights assigned to the different terms in the loss function. We present a comprehensive study of these weight coefficients in the Supplementary material<sup>3</sup>. However, the encoder captures all the landmark transformations *only* in the 2D image plane, because the geometric transforms used in  $\mathcal{R}_g$  and in the discriminator are both 2D transforms. Hence, the future work will entail extension of these transforms into 3D domain, which is expected to significantly boost performance on those faces that look up/down/sideways or have a weird viewangle.

Moreover, Figure 5 shows first adaptation of `stylegan2` to conditional generation. In the semi-supervised case, it splits the landmarks and the style data exceptionally well, so that we can generate fake photos of a person (the fixed style) from different sets of landmarks. We find BRULÉ to be well positioned for regularization in active learning (AL) frameworks to gain efficient annotation strategies [23]. AL and multi-class barycenters are both obvious extensions for the future work. This effort paves the way towards the vision of complete image understanding with no supervision.

<sup>2</sup>Yet, the negligible effect of the barycenter on the *supervised* training was confirmed experimentally.

<sup>3</sup>Also: the extra meaning behind the terms in the loss function, e.g., how to avoid collapse of landmarks.



## Broader Impact

Complete understanding of a scene in an image is the ultimate goal of the ‘smart’ computer vision algorithms. To move in the direction of that vision, it is natural to begin the comprehension from extracting some smaller scene components which constitute the image. Carrying out such decomposition into individual parts (a.k.a., segmentation) *in a completely unsupervised manner* is what motivated our work. Herein, we have solved this task for somewhat of a simpler problem: unsupervised landmark detection, which could be considered as the first step towards the bigger goal.

We demonstrate the efficiency of the method on the datasets that contain images of faces, with the segmentation implying extraction of the facial landmarks (key-points). One of our most striking ‘firsts’ is that this key-point extraction is *100% interpretable*. An immediate practical impact is expected in the areas of video and image editing, where detection/selection of the contours of an object could be done automatically. Painting over an object, changing the style of an object in a scene, combining various objects from different sources in one picture – all of these areas have acquired a powerful tool into their arsenal.

As another important impact of our work, the BRULÉ approach will become extremely useful in the biomedical field. In the clinical setting, where one requires high accuracy of the per-pixel image predictions to support the diagnostic decisions, only specialists from the field can perform the essential annotations, significantly slowing down the time for obtaining a marked dataset. However, our method relies on the use of barycenters (the ‘average image’ values), effectively allowing us to address this problem: because the same organ is quite similar among different patients, computing the average barycenter is a very sensible endeavor to generalize among large patient cohorts. Our method will change the way the anatomic segmentation is approached when there is a limited amount of annotated data.

## Acknowledgements

We thank Ivan Oseledets and Victor Lempitsky for helpful discussions.

## References

- [1] Nicolas Bonneel, Gabriel Peyré, and Marco Cuturi. Wasserstein barycentric coordinates: Histogram regression using optimal transport. *ACM Transactions on Graphics*, 35(4):71:1–71:10, April 2016.
- [2] Nazar Buzun. Gaussian approximation for empirical barycenters. *arXiv*, 1904.00891, 2019.
- [3] Oya Celiktutan, Sezer Ulukaya, and Bülent Sankur. A comparative study of face landmarking techniques. *EURASIP Journal on Image and Video Processing*, 2013:1–27, 2013.
- [4] Liang-Chieh Chen, Yukun Zhu, George Papandreou, Florian Schroff, and Hartwig Adam. Encoder-decoder with atrous separable convolution for semantic image segmentation. *CoRR*, abs/1802.02611, 2018.
- [5] Aritra Chowdhury, Dmitry V Dyllov, Qing Li, Michael MacDonald, Dan E Meyer, Michael Marino, and Alberto Santamaria-Pang. Blood vessel characterization using virtual 3d models and convolutional neural networks in fluorescence microscopy. In *ISBI 2017*, pages 629–632. IEEE, 2017.
- [6] Timothy F. Cootes, Gareth J. Edwards, and Christopher J. Taylor. Active appearance models. *IEEE Trans. Pattern Anal. Mach. Intell.*, 23(6):681–685, June 2001.
- [7] David Cristinacce and Tim Cootes. Automatic feature localisation with constrained local models. *Pattern Recogn.*, 41(10):3054–3067, October 2008.
- [8] Zhen-Hua Feng, Josef Kittler, Muhammad Awais, Patrik Huber, and Xiaojun Wu. Wing loss for robust facial landmark localisation with convolutional neural networks. *CoRR*, abs/1711.06753, 2017.
- [9] Kaiming He, Georgia Gkioxari, Piotr Dollár, and Ross B. Girshick. Mask R-CNN. *CoRR*, abs/1703.06870, 2017.
- [10] Xun Huang, Ming-Yu Liu, Serge J. Belongie, and Jan Kautz. Multimodal unsupervised image-to-image translation. *CoRR*, abs/1804.04732, 2018.
- [11] Tomas Jakab, Ankush Gupta, Hakan Bilen, and Andrea Vedaldi. Unsupervised learning of object landmarks through conditional image generation. pages 4016–4027, 2018.
- [12] Tomas Jakab, Ankush Gupta, Hakan Bilen, and Andrea Vedaldi. Learning landmarks from unaligned data using image translation. *CoRR*, abs/1907.02055, 2019.
- [13] Xu Ji, João F. Henriques, and Andrea Vedaldi. Invariant information distillation for unsupervised image segmentation and clustering. *CoRR*, abs/1807.06653, 2018.
- [14] Asako Kanezaki. Unsupervised image segmentation by backpropagation. In *Proceedings of IEEE International Conference on Acoustics, Speech, and Signal Processing (ICASSP)*, 2018.
- [15] Tero Karras, Samuli Laine, Miika Aittala, Janne Hellsten, Jaakko Lehtinen, and Timo Aila. Analyzing and improving the image quality of StyleGAN. *CoRR*, abs/1912.04958, 2019.
- [16] Wei Liu, Dragomir Anguelov, Dumitru Erhan, Christian Szegedy, Scott Reed, Cheng-Yang Fu, and Alexander C. Berg. Ssd: Single shot multibox detector. 2016. To appear.
- [17] Ziwei Liu, Ping Luo, Xiaogang Wang, and Xiaoou Tang. Deep learning face attributes in the wild. In *Proceedings of International Conference on Computer Vision (ICCV)*, December 2015.
- [18] Alejandro Newell, Kaiyu Yang, and Jia Deng. Stacked hourglass networks for human pose estimation. *CoRR*, abs/1603.06937, 2016.
- [19] Pavel Ostyakov, Roman Suvorov, Elizaveta Logacheva, Oleg Khomenko, and Sergey I. Nikolenko. Seigan: Towards compositional image generation by simultaneously learning to segment, enhance, and inpaint. Arxiv preprint arXiv:1811.07630 [cs.CV], 2018.
- [20] B.T. Polyak. Vvedenie v optimizatsiyu. *Moscow: Nauka, 1983. Translated into English under the title Introduction to Optimization, New York: Optimization Software, 1987.*
- [21] Denis Prokopenko, Joël Valentin Stadelmann, Heinrich Schulz, Steffen Renisch, and Dmitry V Dyllov. Unpaired synthetic image generation in radiology using gans. In *Artificial Intelligence in Radiation Therapy, MICCAI*, pages 94–101. Springer, Cham, 2019.
- [22] C. Sagonas, G. Tzimiropoulos, S. Zafeiriou, and M. Pantic. 300 faces in-the-wild challenge: The first facial landmark localization challenge. In *2013 IEEE International Conference on Computer Vision Workshops*, pages 397–403, 2013.

- [23] Artem Shelmanov, Vadim Liventsev, Danil Kireev, Nikita Khromov, Alexander Panchenko, Irina Fedulova, and Dmitry V Dyllov. Active learning with deep pre-trained models for sequence tagging of clinical and biomedical texts. In *2019 IEEE International Conference on Bioinformatics and Biomedicine (BIBM)*, pages 482–489. IEEE, 2019.
- [24] Nikolay Shvetsov, Nazar Buzun, and Dmitry V Dyllov. Unsupervised non-parametric change point detection in quasi-periodic signals. *arXiv preprint arXiv:2002.02717*, 2020.
- [25] Y. Sun, X. Wang, and X. Tang. Deep convolutional network cascade for facial point detection. pages 3476–3483, 2013.
- [26] J. Thewlis, S. Albanie, H. Bilen, and A. Vedaldi. Unsupervised learning of landmarks by exchanging descriptor vectors.
- [27] James Thewlis, Hakan Bilen, and Andrea Vedaldi. Unsupervised learning of object landmarks by factorized spatial embeddings. *CoRR*, abs/1705.02193, 2017.
- [28] James Thewlis, Hakan Bilen, and Andrea Vedaldi. Unsupervised object learning from dense equivariant image labelling. *CoRR*, abs/1706.02932, 2017.
- [29] Olivia Wiles, A. Sophia Koepke, and Andrew Zisserman. Self-supervised learning of a facial attribute embedding from video. *CoRR*, abs/1808.06882, 2018.
- [30] Xide Xia and Brian Kulis. W-net: A deep model for fully unsupervised image segmentation. *CoRR*, abs/1711.08506, 2017.
- [31] Shengtao Xiao, Jiashi Feng, Junliang Xing, Hanjiang Lai, Shuicheng Yan, and Ashraf Kassim. Robust facial landmark detection via recurrent attentive-refinement networks. 9905:57–72, 10 2016.
- [32] Zhanpeng Zhang, Ping Luo, Chen Change Loy, and Xiaoou Tang. Learning and transferring multi-task deep representation for face alignment. *CoRR*, abs/1408.3967, 2014.
- [33] Hengshuang Zhao, Jianping Shi, Xiaojuan Qi, Xiaogang Wang, and Jiaya Jia. Pyramid scene parsing network. *CoRR*, abs/1612.01105, 2016.
- [34] Jun-Yan Zhu, Taesung Park, Phillip Isola, and Alexei A. Efros. Unpaired image-to-image translation using cycle-consistent adversarial networks. *CoRR*, abs/1703.10593, 2017.

# BRULÉ: Barycenter-Regularized Unsupervised Landmark Extraction Supplemental material

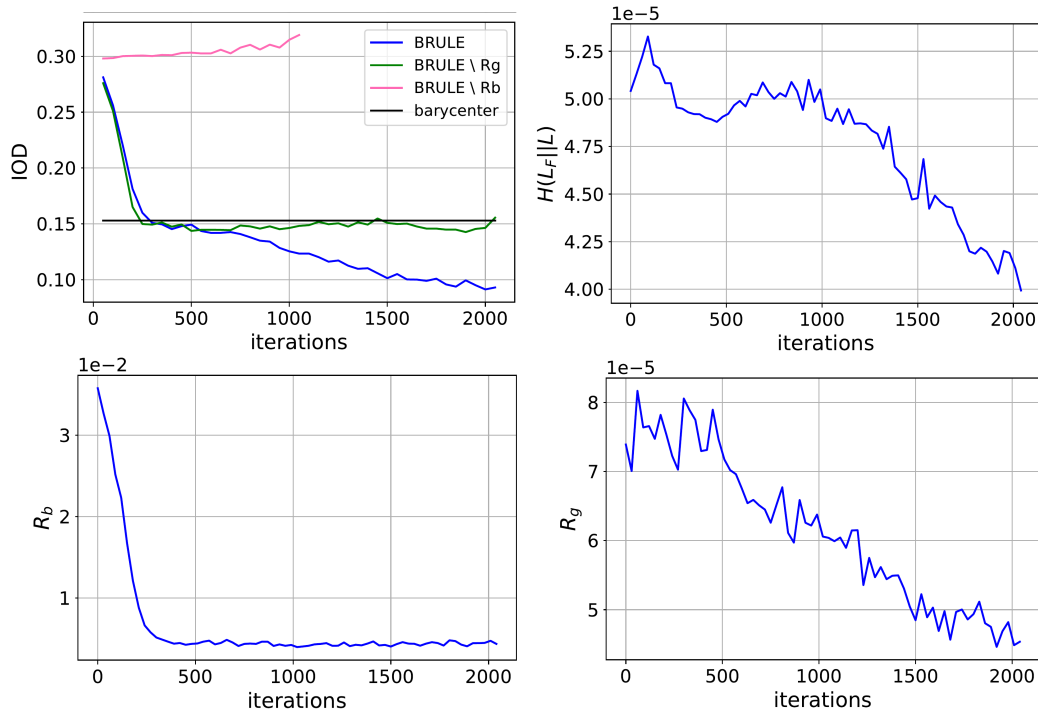


Figure 6: BRULÉ ablation study using Inter Ocular Distance as the metric (IOD).

*Top left:* The value of the barycenter is the black curve. BRULÉ with omitted regularization  $R_b$  fails to reach the barycenter. BRULÉ with omitted  $R_g$  is already capable of improving the IOD beyond the barycenter (green). All six components of the loss function contribute to the landmark detection performance beyond the barycenter (blue).

*Top right:* Behaviour of individual loss contribution of cross-entropy  $H(L_F||L)$  between the fake and the predicted landmarks.

*Bottom row:* Individual contributions of the regularizing loss components  $R_b$  and  $R_g$ .

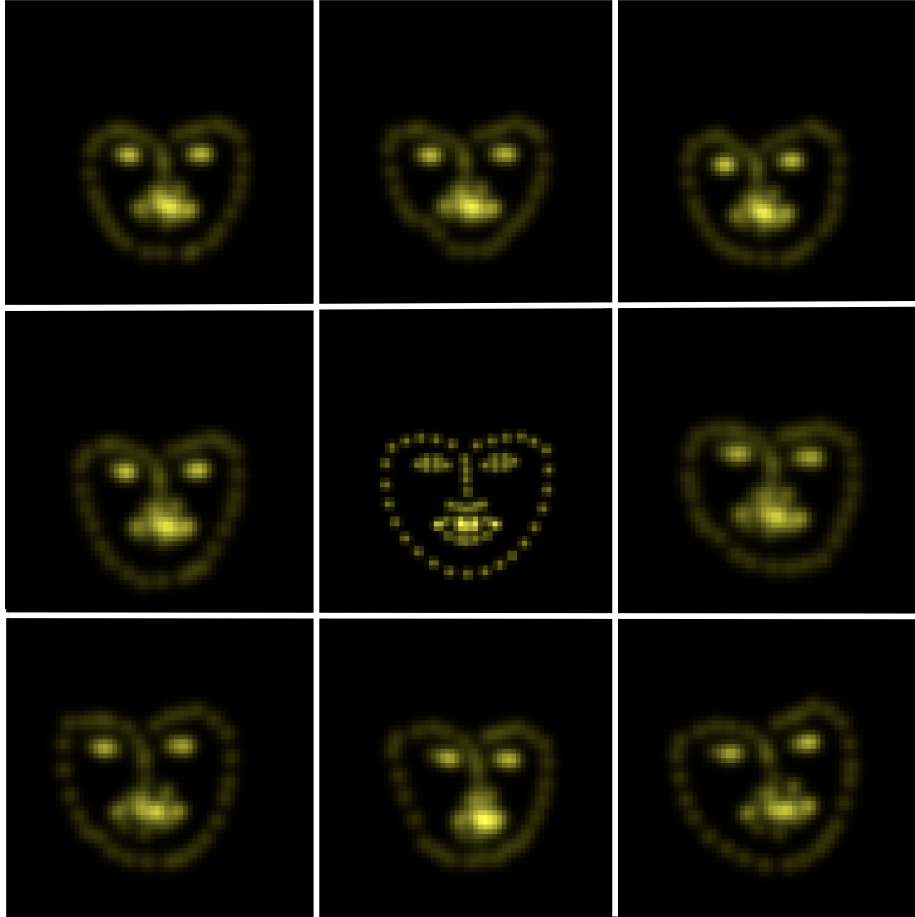


Figure 7: The central image is the barycenter computed on the entire dataset. To calculate deformations required to transport each given face to such barycenter, individual landmark heatmaps are calculated. The heatmaps are shown for 8 random faces from the dataset. They are blurred because of the mapping into the mixture of Gaussian measures.

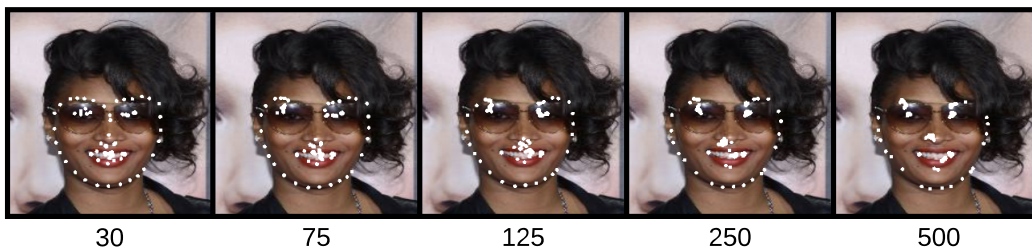


Figure 8: Example of the collapse of landmarks discussed in the main text. Our loss components allow to avoid the collapse into the barycenter and into the clusters of points as shown here. The frame labels correspond to the iteration number.